Numerical modelling of the TALOS wave energy converter - using HydroChrono and Ansys Fluent

David Ogden, Foivos (Phoevos) Koukouvinis, Wanan Sheng, George Aggidis, John Anagnostopoulos and Aidan Bharath

Abstract—**Harnessing the untapped potential of wave energy demands advanced modelling tools that accurately represent wave energy converters (WECs) and facilitate the optimization of their designs. This paper introduces two new numerical models of the TALOS WEC concept currently under development by Lancaster University, UK [1]. In this project we employ HydroChrono - a fully open-source hydrodynamics package for the open-source multi-body dynamics software, Project Chrono [2]. HydroChrono enables potential flow-based modelling of WECs and offers the flexibility to explore various design configurations, which is demonstrated in the results section.**

Confidence in our model's accuracy is established via comparisons with Computational Fluid Dynamics (CFD) simulations, performed with Ansys Fluent. HydroChrono enables us to vary key design parameters of the TALOS WEC, including mass distribution and Power Take-Off (PTO) properties - which can offer insights for future design improvements.

Looking ahead, the application of HydroChrono for WEC numerical modelling offers pathways to more sophisticated analyses. This includes potential integration with the MoorDyn package for nonlinear mooring dynamics, and the possibility of detailed hydraulic drivetrain modeling. These developments facilitate more detailed performance prediction and system optimization for wave energy conversion technology, leading to more cost-effective and efficient marine renewable energy solutions.

Index Terms—**Wave Energy, Numerical Modeling, CFD, Potential Flow, TALOS**

I. Introduction

A. Background & motivation

TALOS, a point absorber-style Wave Energy Converter (WEC), originated as a concept and initial development within Lancaster University, UK. The TALOS WEC includes a multi-axis Power Take-Off (PTO) system, comprised of a heavy internal reaction mass (IRM) nested within the WEC's hull and supported by spring-dampers.

The multi-axis approach of this wave energy converter allows energy to be extracted from multiple movement modes of the structure amidst waves, thus enhancing the energy extraction efficiency. During this energy transformation, the IRM maintains relative stability while the structure's motion under wave forces results in relative movement between the structure and the ball. This relative motion propels the PTO elements (including springs and dampers) to convert wave energy into useful mechanical energy. The TALOS WEC benefits from a completely enclosed PTO within the structure, with no moving parts exposed to seawater.

The TALOS multi-axis wave energy converter technology, or 'NHP-WEC' in shorthand, was chosen among eight projects supported by UK Research and Innovation (UKRI) to tap into the enormous potential of ocean wave energy. The key objectives of the NHP-WEC project are to refine the TALOS WEC and the associated PTO system, and to further WEC technology by creating essential control and monitoring systems for the device.

Furthermore, in 2023, Lancaster University began collaborating with the National Renewable Energy Laboratory (NREL) under the US Department of Energy's (DoE) Water Power Technology Office (WPTO) TEAMER program - to develop numerical models of the TALOS WEC that could help improve the system's design.

II. Methods

A. HydroChrono

HydroChrono (https://github.com/NREL/HydroChrono) is a novel numerical modeling package developed for simulating Wave Energy Converters (WECs) and designed to work seamlessly with the open-source physics engine, Project Chrono. A screenshot of the code is shown in Figure 1

HydroChrono essentially makes two modifications to Chrono's multibody dynamics equations - it adds a dense added mass matrix (A) to the system's mass matrix and includes an additional 'hydrodynamic force vector', $F_h(\dot{q}, q, t)$:

$$(M(q) + A)\ddot{q} + \Phi_q^T(q)\lambda = Q(\dot{q}, q, t) + F_h(\dot{q}, q, t) \quad (1)$$

© 2023 European Wave and Tidal Energy Conference. This paper has been subjected to single-blind peer review.

This work was authored in part by the National Renewable Energy Laboratory, for the U.S. Department of Energy (DOE) under Contract No. DE-AC36-08GO28308. The views expressed in the article do not necessarily represent the views of the DOE or the U.S. Government. This work was partially funded by the UK EPSRC (grant number EP/V040561/1) 'Novel High Performance Wave Energy Converters with advanced control, reliability and survivability systems machine-learning forecasting (NHP-WEC)' for the TALOS project.

David Ogden and Aidan Bharath are with the National Renewable Energy Laboratory, 5013 Denver West Parkway, Golden, CO 80401 U.S. (e-mail: david.ogden.nrel@outlook.com, aidan.bharath@nrel.gov).

Foivos (Phoevos) Koukouvinis and John Anagnostopoulos are with the National Technical University of Athens (NTUA), School of Mechanical Engineering, Athens, Greece (e-mail: fivoskouk@gmail.com, anagno@fluid.mech.ntua.gr).

Wanan Sheng and George Aggidis are with Lancaster University, School of Engineering, Lancaster, UK.

Digital Object Identifier: https://doi.org/10.36688/ewtec-2023-532

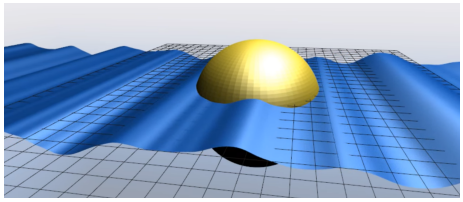

Figure 1. Demonstration of a floating body in irregular waves, simulated with HydroChrono.

$F_h(\dot{q}, q, t)$ has several components, including the hydrostatic force $F_{hs}(q)$, radiation damping force $F_{rad}(\dot{q}, q)$, and wave excitation force $F_{exc}(t)$:

$$F_h(\dot{q}, q, t) = F_{hs}(q, t) + F_{rad}(\dot{q}, t) + F_{exc}(t) \quad (2)$$

The hydrostatic force, $F_{hs}(q, t)$ represents the restoring force due to buoyancy and changes in the body's waterplane area, and is given by:

$$F_{hs}(q, t) = K_h \Delta q = K_h(q - q_0) \quad (3)$$

The radiation damping force, $F_{rad}(\dot{q}, t)$ can be obtained through a convolution integral between the radiation impulse response function $K_{rad}(t)$ and the system's velocity history $\dot{q}(\tau)$:

$$F_{rad}(\dot{q}, t) = \int_{-\infty}^{t} K_{rad}(t - \tau)\dot{q}(\tau)d\tau \quad (4)$$

The wave excitation force, $F_{exc}(t)$ is computed via convolution between the excitation impulse response function $K_{exc}(t)$ and the wave elevation time series $\eta(t)$:

$$F_{exc}(t) = \int_{-\infty}^{+\infty} K_{exc}(\tau)\eta(x, y, t - \tau)d\tau \quad (5)$$

The hydrostatic stiffness matrix K_h, and the impulse response functions K_{rad} and K_{exc} can all be obtained from open-source boundary element method (BEM) codes. In this project we used Capytaine [3] to compute these data.

B. CFD Modelling

The CFD modelling of the TALOS buoy was performed using ANSYS® Fluent, Release 2021R2, as an Unsteady Reynolds Averaged Navier Stokes (URANS) simulation. The simulation involves solving the pressure equation enforcing continuity, the momentum equations (including gravity, acting towards the -Z direction, as shown in Figure 2), the phase field equation to track the free surface and the turbulence closure. Here, the $k-\omega$ SST turbulence model was used, due to its generality. The TALOS buoy motion is tracked with rigid body kinematics; here only constrained motion at the vertical (Z) direction or constrained rotation at the X-axis, around the center of gravity, was examined, hence kinematics are reduced to a simple equation, in the form of the Newton law of motion, which is integrated in time, implicitly coupled with the fluid flow.

The computational domain spans in a rectangular box of dimensions 1km x 1km x 200m, as shown in Figure 2; this rectangular domain is the background zone used to map the moving overset spherical domain, which includes the TALOS buoy, as shown in the magnified insert of Figure 2. The boundary conditions involve a stationary wall boundary condition at the bottom of the rectangular domain, symmetry boundary conditions at the sides of the rectangular domain and fixed pressure at the top boundary. The boundary of the spherical moving zone is an overset interface, coupled with the background rectangular domain.

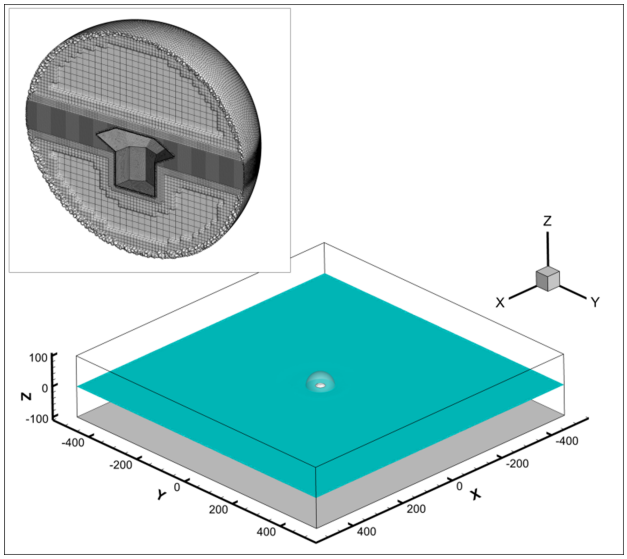

Figure 2. Illustration of the CFD simulation set-up. The computational domain is shown at the bottom part of the image; it consists of a rectangular box of 1km x 1km x 200m, which is the background mesh zone. They grey surface denotes the bottom (wall boundary), whereas the cyan surface is the initial location of the air/water interface. The spherical domain near the center of the rectangular box is the overset zone, which is shown as a magnified insert at the top left of the image. The computational mesh of the overset zone is also shown, demonstrating the refinement near the TALOS buoy and the expected location of the free surface.

The spatial discretisation varies depending on the location and the features of interests; near the TALOS buoy and the location of the air/water interface it is 0.325m. Moreover, five inflation cell layer are placed at the surface of the TALOS buoy, to capture boundary layers. Resolution gradually coarsens with moving away from the area of interest, to a cell size of 2.5m. This coarsening allows to save computational resources and dampen any emitted surface waves which otherwise would reflect a the side boundaries and affect the TALOS motion. The time step used was 0.05s, which is at least 100-times smaller than the time-scale (period) of oscillation for the type of motion examined in the present study (which is roughly 5-10s). The time window of the simulation was in the order of 30s, after which the motion of the TALOS buoy has completely decayed.

Indicative instances of the simulation examining the decay of vertical heave motion, with an initial displacement +3m at the vertical direction, are shown in Figure 6. As shown in the instances, at the beginning (1s) the buoy moves downwards, reaching a minimum at roughly 3s. Then the buoy moves upwards (see 5s) dragging water with it, completing a period of oscillation at 6.93s. The oscillation repeats with a decaying rate, up to 30s, where the maximum velocity has dropped to roughly 4cm/s (or almost 2% of the maximum velocity, near the beginning of the simulation).

C. TALOS model description & input data

Before simulating TALOS in the time-domain, the open-source BEM code Capytaine [3] was used to compute hydrodynamic coefficients in the frequency domain. The mesh used by Capytaine is shown in Figure 3 The main properties of the TALOS WEC are shown in Table I.

Table I. TALOS system properties.

Property	Value	Units
Total Mass	$3.748 \cdot 10^6$	kg
Water Density	998.2	kg/m^3
Hull CoG	$\begin{bmatrix} 0.0 \\ 0.0 \\ -7.96 \end{bmatrix}$	m
Hull Inertia	$\begin{bmatrix} 2.376 \cdot 10^8 & 0 & 0 \\ 0 & 2.376 \cdot 10^8 & 0 \\ 0 & 0 & 2.376 \cdot 10^8 \end{bmatrix}$	kgm^2
IRM CoG	$\begin{bmatrix} 0.0 \\ 0.0 \\ -5.70 \end{bmatrix}$	m
IRM Inertia	$\begin{bmatrix} \frac{2}{5}mr^2 & 0 & 0 \\ 0 & \frac{2}{5}mr^2 & 0 \\ 0 & 0 & \frac{2}{5}mr^2 \end{bmatrix}$	kgm^2

Additional detail about the PTO attachment points and rest lengths is presented in table II

Table II. Attachment points and rest lengths for each PTO in the TALOS system.

PTO #	Attachment Point (m) Hull	IRM	Rest length (m)
1	$\begin{bmatrix} 5.000 \\ 0.000 \\ -8.660 \end{bmatrix}$	$\begin{bmatrix} 2.500 \\ 0.000 \\ -4.330 \end{bmatrix}$	5.0
2	$\begin{bmatrix} -2.500 \\ 4.330 \\ -8.660 \end{bmatrix}$	$\begin{bmatrix} -1.250 \\ 2.165 \\ -4.330 \end{bmatrix}$	5.0
3	$\begin{bmatrix} -2.500 \\ -4.330 \\ -8.660 \end{bmatrix}$	$\begin{bmatrix} -1.250 \\ -2.165 \\ -4.330 \end{bmatrix}$	5.0
4	$\begin{bmatrix} 5.000 \\ 0.000 \\ 8.660 \end{bmatrix}$	$\begin{bmatrix} 2.500 \\ 0.000 \\ 4.330 \end{bmatrix}$	2.0
5	$\begin{bmatrix} -2.500 \\ 4.330 \\ 8.660 \end{bmatrix}$	$\begin{bmatrix} -1.250 \\ 2.165 \\ 4.330 \end{bmatrix}$	2.0
6	$\begin{bmatrix} -2.500 \\ -4.330 \\ 8.660 \end{bmatrix}$	$\begin{bmatrix} -1.250 \\ -2.165 \\ 4.330 \end{bmatrix}$	2.0

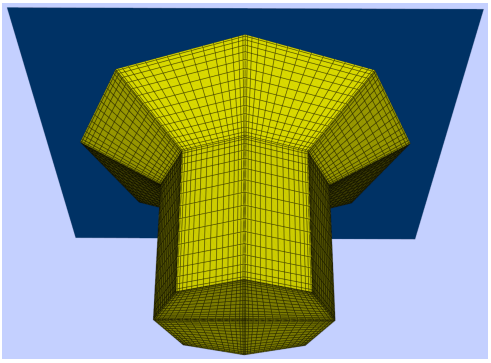

Figure 3. TALOS hydrodynamic mesh used in the BEM code, Capytaine.

III. Results & Analysis

A. Decay test validation results

In order to validate that the hydrodynamic characteristics of the TALOS WEC hull are being accurately captured by Capytaine and HydroChrono, decay tests were compared to the CFD results from Ansys Fluent.

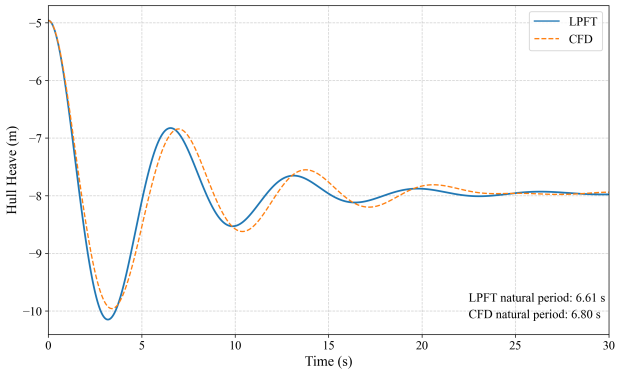

Figure 4. TALOS heave decay test results - HydroChrono (PTOs locked) versus Ansys Fluent.

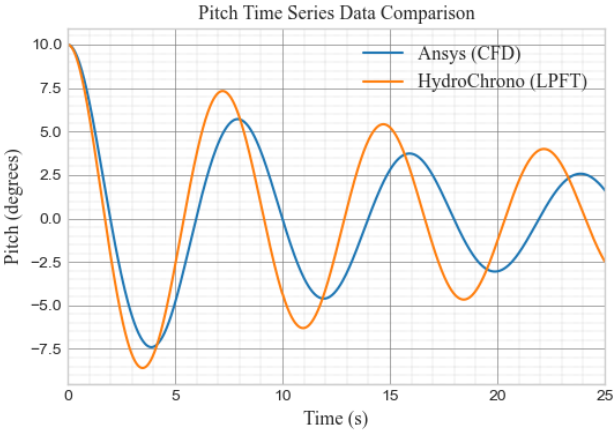

Figure 5. TALOS pitch decay test results - HydroChrono (PTOs locked) versus Ansys Fluent.

The natural period of each time series was determined by finding the average time between peaks of the time series - using the `scipy.signal.find_peaks` function, which

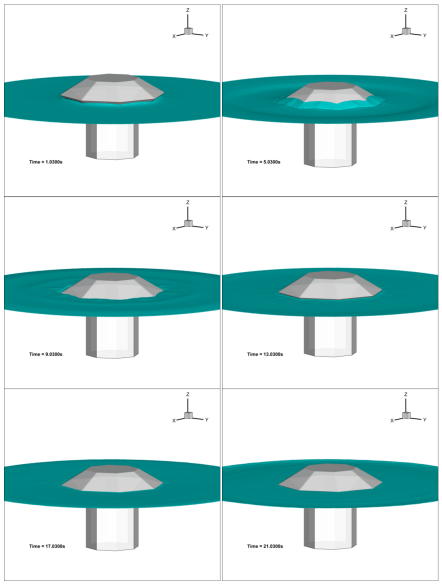

Figure 6. TALOS heave decay test - CFD visualization.

identifies the local maxima in a 1-D array; where `x[i] > x[i-1]` and `x[i] > x[i+1]`. The difference between consecutive peak indices is taken to get the number of time steps between peaks.

The natural period T is then computed as the average of these time differences:

$$T = \frac{1}{n}\sum_{i=1}^{n}(t_{i+1} - t_i) \tag{6}$$

For the heave decay tests, the natural period was found to be $6.6s$ in HydroChrono and $6.8s$ in Ansys Fluent - a 3.0% error. For the pitch decay tests, the natural period was found to be $7.2s$ in HydroChrono and $7.9s$ in Ansys Fluent - a 9.7% error. As shown in Figures 4 and 5, the agreement is much better in the heave degree of freedom. In pitch, the lack of viscous damping in the HydroChrono model is much more evident. This could be due to the sharp corners of the TALOS geometry having a more pronounced effect in the pitch degree of freedom. In future work we will include an approximate viscous damping force in the HydroChrono model to capture this additional damping.

B. Using HydroChrono as a Design Tool

The validation cases comparing HydroChrono to CFD results only considered the system as a single body - i.e. the PTO's are 'locked' in that configuration. In this section the PTOs are unlocked to enable relative motion between the two bodies and thus power production. The 6 PTOs are all modelled as linear spring-dampers, as shown in Figure 7. Modelling the PTOs enables us to start evaluating some of the design parameters in the system and exploring how they impact TALOS' performance.

Figure 8 shows that at t=0s, the IRM drops slightly, as the PTO spring-dampers are not in equilibrium - i.e. the compression forces on the lower PTOs are greater

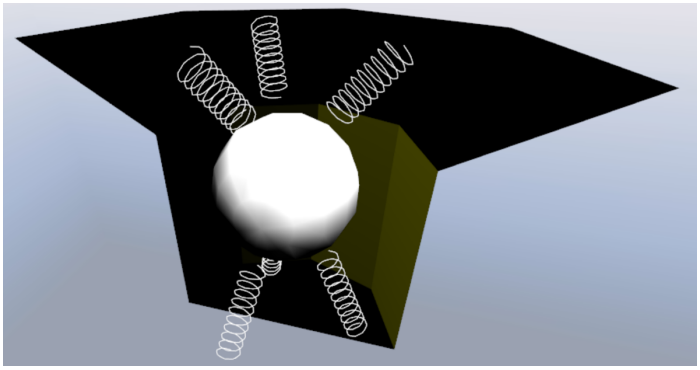

Figure 7. Screenshot of the multibody TALOS system modeled with HydroChrono. This is a cutaway view of the system, to show the internal mechanical system.

than the tension forces on the upper PTOs. Figure 8 shows how increasing the stiffness of the PTOs helps to limit this drop.

The other key factor determining the pre-tension on the PTOs is their rest length, which is defined in Table II. The pre-tension/stiffness trade-off is critical to better understand the characteristics of the TALOS WEC and should be explored more thoroughly in future work. The main factor that these parameters influence is the equilibrium position of the IRM. The importance/influence of the IRM position also needs to be explored further and better understood in future work.

To explore how the PTO stiffness and damping influence the performance of the TALOS system, power response curves were generated for each configuration across a range of different wave periods. This simply takes the average of the aggregate power from all 6 PTOs produced in regular waves - once the system has reached a steady-state response.

Figure 9 shows the PTO stiffness term increasing with each subplot. For each PTO stiffness value, various PTO damping coefficients were simulated, and the power response curves have been obtained for each combination.

The general trend observed in Figure 9 is that as we make the system stiffer, we flatten the power response curve. Furthermore, the highest damping coefficients simulated tend to perform better in the stiffer systems than the less-stiff systems, where the ideal damping coefficients were around $1.20 \cdot 10^6 Ns/m$.

Another important design parameter for the TALOS system is the mass distribution between hull and IRM. For a PTO stiffness of $1.0 \cdot 10^6 N/m$ and a PTO damping of $1.20 \cdot 10^6 Ns/m$, 3 different mass distributions have been simulated (hull:IRM): 80:20, 70:30 and 60:40 - as shown in Figure 10.

From Figure 10 we can see that the 80:20 mass ratio produces the most noticeable peak, whereas the more even mass distributions seem to flatten the power response curve. These broader, flatter responses could be due to the system being over-damped in these configurations. Ideally, all of these parameters should be explored in conjunction in order to fully understand

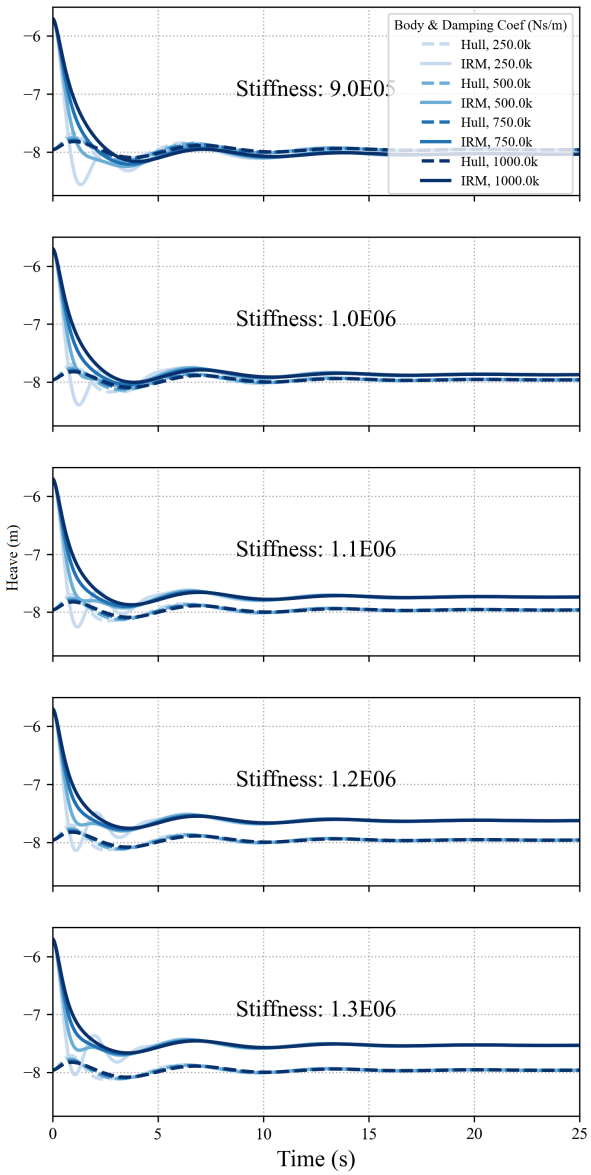

Figure 8. Still water results for the 2-body system, showing the IRM dropping various amounts (depending on PTO stiffness) at t=0s, due to the upper and lower PTOs not being in equilibrium.

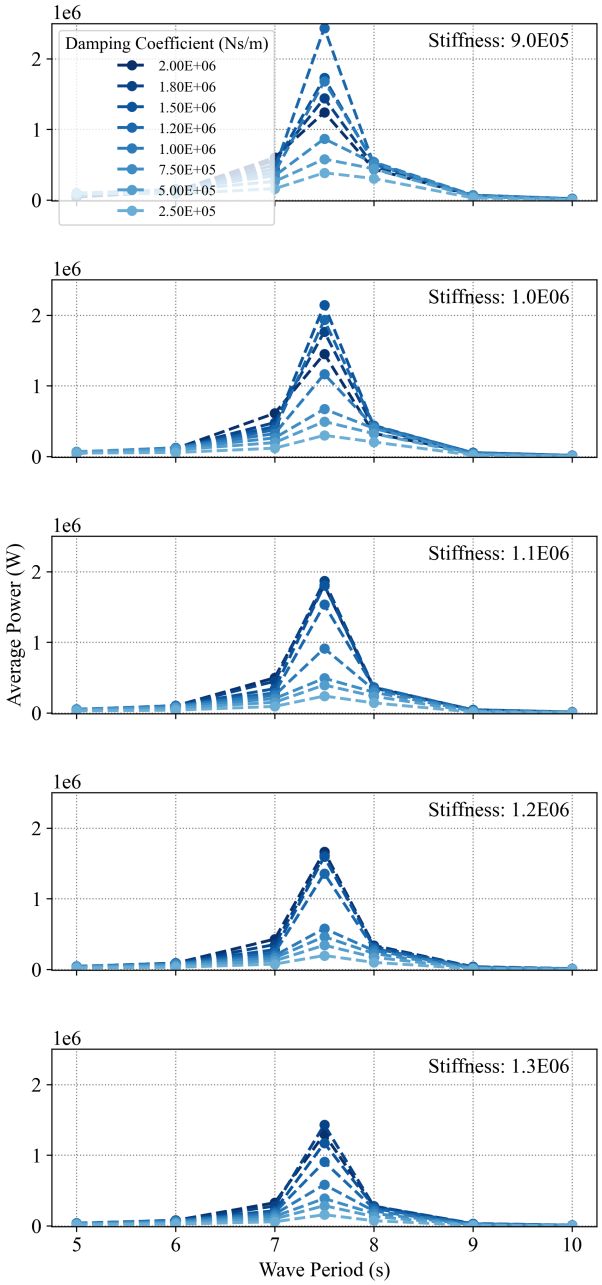

Figure 9. Power response curves - varying the TALOS WEC's PTO stiffness and damping coefficients.

the system's characteristics and produce an optimal design.

IV. Discussion, Conclusions & Future Work

In this paper we presented a numerical model of the TALOS WEC using HydroChrono, a new, fully open-source hydrodynamic package for Project Chrono. The model results have been compared to Ansys Fluent (CFD) results for the case where the PTOs are locked. Very good agreement has been observed in the heave degree of freedom, but the pitch decay test results highlight the need to approximate viscous drag effects in HydroChrono - which is planned future work.

The HydroChrono model has also been run with 'unlocked' PTOs in the system, to permit relative motion between the two bodies (hull and IRM) and approximate the power being absorbed by the spring-dampers.

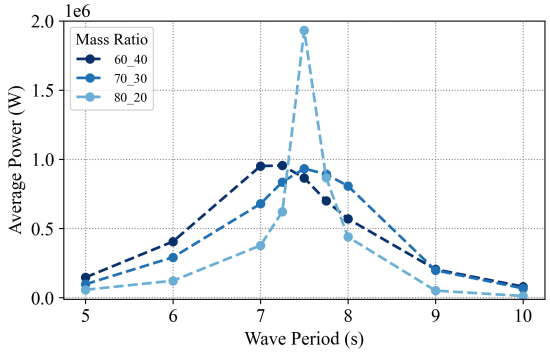

Figure 10. Power response curves - varying the mass ratio between the TALOS WEC's hull and IRM.

The initial tests with this model simply simulated the system in still water to ensure static equilibrium. However, we observed that the IRM was not in equilibrium in its initial position, and it dropped slightly. By increasing the stiffness of the PTOs, we observed that the amount the IRM drops can be reduced. However, in Figure 9, we show that the PTO stiffness impacts power production and generally the less stiff configurations absorb more power (as expected). From Figure 9 we can see that as the PTO stiffness varies, the ideal PTO damping coefficient also changes.

Another option to prevent the IRM from dropping at $t = 0s$ without increasing the stiffness of the PTO would be to change the pre-tension of the PTO spring-dampers - by changing their rest length values. However, its important to bear in mind that the optimal IRM position has also not yet been determined - and will almost certainly change depending on the other system variables.

Another design variable explored in this paper is the mass ratio between hull and IRM. Our results seem to indicate that a lighter IRM produces a narrower, peakier response, whereas a heavier IRM produces a more damped, broad banded response 10.

Examining how all of these variables influence the performance of the TALOS WEC by varying them simultaneously could yield valuable information about the optimal TALOS system configuration. Hence, future work should seek to perform this type of multivariate optimization study.

Furthermore, increasing the complexity of the HydroChrono model - including a viscous drag approximation, nonlinear mooring system, and hydraulic drivetrain PTO would all be valuable improvements that could help to better understand and optimize the TALOS WEC.

REFERENCES

[1] G. Aggidis and C. Taylor, "Overview of wave energy converter devices and the development of a new multi-axis laboratory prototype," *IFAC-PapersOnLine*, vol. 50, no. 1, pp. 15 651–15 656, 2017, 20th IFAC World Congress. [Online]. Available: https://www.sciencedirect.com/science/article/pii/S240589631733210X

[2] A. Tasora, R. Serban, H. Mazhar, A. Pazouki, D. Melanz, J. Fleischmann, M. Taylor, H. Sugiyama, and D. Negrut, "Chrono: An open source multi-physics dynamics engine," in *High Performance Computing in Science and Engineering*, T. Kozubek, R. Blaheta, J. Šístek, M. Rozložník, and M. Čermák, Eds. Cham: Springer International Publishing, 2016, pp. 19–49.

[3] M. Ancellin and F. Dias, "Capytaine: a python-based linear potential flow solver," *Journal of Open Source Software*, vol. 4, no. 36, p. 1341, 2019. [Online]. Available: https://doi.org/10.21105/joss.01341